Extreme structural stability of Ti0.5Sn0.5O2 nanoparticles: synergistic effect in the cationic sublattice

Denis Machon, Sylvie Le Floch, Shashank Mishra, Stéphane Daniele, Karine Masenelli-Varlot, Patrick Hermet, Patrice Mélinon

Extreme structural stability of $Ti_{0.5}Sn_{0.5}O_2$ nanoparticles: synergistic effect in the cationic sublattice†

Denis Machon, *[a,b] Sylvie Le Floch, [a] Shashank Mishra, [c] Stéphane Daniele, [c] Karine Masenelli-Varlot, [d] Patrick Hermet [e] and Patrice Mélinon [a]

$Ti_{0.5}Sn_{0.5}O_2$ nanoparticles (~5 nm and ~10 nm) have been studied under high pressure by Raman spec-troscopy. For particles with diameter ~10 nm, a transformation has been observed at 20–25 GPa while for particles with ~5 nm diameter no phase transition has been observed up to ~30 GPa. The $Ti_{0.5}Sn_{0.5}O_2$ solid solution shows an extended stability at the nanoscale, both of its cationic and anionic sublattices. This ultrastability originates from the contribution of Ti and Sn mixing: Sn stabilizes the cationic network at high pressure and Ti ensures a coupling between the cationic and anionic sublattices. This result ques-tions a "traditional" crystallographic description based on polyhedra packing and this synergistic effect reported in this work is similar to the case of metamaterials but at the nanoscale.

At the nanoscale, the phase stability of a system is often modified compared to the bulk. The thermodynamics and kinetics of phase transitions are strongly impacted by the contribution of the interface energy and some additional size effects (confinements, molecular effect, *etc.*).[1] For example, under ambient conditions, polymorphs that differ from the bulk counterpart can be stabilized in nanostructures. This is a typical size-induced phase transition, as reported for Ni[2] or for TiO_2.[3] In the latter case, the anatase-type structure (space group #141, $I4_1/amd$) is observed in nanoparticles while a rutile-type structure (space group #136, $P4_2/mnm$) is the stable polymorph for the bulk. Likewise, temperature- or pressure-induced phase transitions in nanomaterials often show significant differences with the bulk. For example, the melting temperature of a compound appeared to depend on the inverse radius of the particles.[4,5] More recently, pressure-induced phase transformations have attracted particular interest because, unlike some high temperature experiments, particle size is not affected by growth and coarsening. The seminal works of Tolbert and Alivisatos showed that the transition pressure can also vary as a $1/R$-law in some cases [ref. 6 and references therein]. However, more recent works demonstrated that the situation can be more complex depending on the system under investigation. Under pressure, change in transition pressure or high-pressure structures, and sometimes amorphization can be observed.[1,7–9] For instance, with increasing pressure, bulk rutile SnO_2 undergoes the following sequence of structural transitions: rutile-type → $CaCl_2$-type → cubic phase (modified fluorite, space group #205, $Pa\bar{3}$).[10] In the nanopowder, the $CaCl_2$-type phase (space group #58, *Pnnm*) has not been observed and the transformation to the high-pressure cubic phase is strongly dependent on the particle size.[11] The cubic structure appeared above 23 GPa, 29 GPa and 30 GPa for bulk, 14 nm and 8 nm SnO_2 samples, respectively. For a particle diameter of 3 nm, no phase transition could be observed at pressures as high as 39 GPa. However, Raman spectroscopy measurements have shown that a pressure-induced disordering of the anionic sublattice starts above 7 GPa in 3 nm diameter particles.[12] Regarding TiO_2, whatever the initial structure (anatase or rutile), a baddeleyite structure (space group #14, $P2_1/c$) has been observed at high pressure, above ~18 GPa.[13,14] Depending on the density of defects in nanoparticles, a high-density amorphous state could be found in place of the baddeleyite structure upon compression.[15–18]

In materials science, another degree of freedom in the Gibbs' phase rule is composition. This led to explore and develop alloys or mixed oxides. In this case as well, size and

[a]*Univ. Lyon, Université Claude Bernard Lyon 1, CNRS UMR 5306, Institut Lumière Matière, F-69622 Villeurbanne, France. E-mail: denis.machon@univ-lyon1.fr*

[b]*Laboratoire Nanotechnologies et Nanosystèmes (LN2), CNRS UMI-3463, Université de Sherbrooke, Institut Interdisciplinaire d'Innovation Technologique(3IT), Sherbrooke, Québec, Canada*

[c]*IRCELYON, CNRS-UMR 5256, Université Lyon 1, 2 Avenue A. Einstein, 69626 Villeurbanne Cedex, France*

[d]*Univ Lyon, INSA Lyon, UCBL, CNRS, MATEIS, UMR 5510, 69621 Villeurbanne, France*

[e]*ICGM, CNRS-UMR 5253, Université de Montpellier, ENSCM, 34090 Montpellier, France*

interfaces play a significant role in the modification of the energy landscape. For instance, the spinodal decomposition observed in some bulk alloys may be bypassed for nanoparticles with radii smaller than a critical value. For example, in the TiO_2–SnO_2 system, the solid solution is stable at high temperature but equimolar systems of TiO_2 and SnO_2 shows demixing to Ti and Sn-rich solids at temperatures below ~1700 K. However, in nanoparticles, such demixing may be bypassed, leading to an extended stability field of the solid solution.[19]

Here, we want to take advantage of this compositional stability at ambient temperature to study the pressure-induced behavior of the $Ti_{0.5}Sn_{0.5}O_2$ solid solution, and to explore the joint effect of pressure and composition in the energy landscape of this system. Using two different particle sizes (~5 and ~10 nm), we demonstrate the size dependence of the transition pressure. The combination of different parameters (size and pressure) allows us to explore the stability fields of the solid solution. In the case of 5 nm particle, the mechanical stability is extremely large compared to the end members. In addition, no decoupling between the cationic and anionic is observed unlike in SnO_2. The high-pressure behavior of these ultrafine nanoparticles allows discussing the respective role of each cation and their synergistic effect and challenge the universality of the traditional crystallographic description based on Pauling's rules.[20]

Methods

Simulations

First-principles based methods were performed within the density functional theory (DFT) framework as implemented in the ABINIT package.[21] The exchange–correlation energy functional was evaluated using the local density approximation parametrized by Perdew and Wang.[22] The all-electron potentials were replaced by norm-conserving pseudopotentials. Sn ($4d^{10}$, $5s^2$, $5p^2$), Ti($3s^2$, $3p^6$, $3d^2$, $4s^2$) and O($2s^2$, $2p^4$)-electrons were considered as valence states. In the case of tin atoms, there is no reason to introduce semi-core electrons because no calculation has shown the importance of introducing semi-cores in a compound. In contrast, the semi-cores ($3s^2$ and $3p^6$) have to be introduced in the construction of the Ti-peudopotential to have reliable results. With semi-core electrons, the calculated structure of TiO_2 is in better agreement with the experimental data than without semi-core electrons. Thus, the semi-core electrons for titanium are mandatory for the calculation of $Ti_{0.5}Sn_{0.5}O_2$ and the results can be compared with the calculated vibrational density-of-states previously published for TiO_2 nanorods.[14] Therefore, nothing in the vibrational or stability properties indicates that a valence transfer or fluctuation should be considered.

The electronic wave functions were expanded in plane-waves up to a kinetic energy cutoff of 65 Ha and integrals over the Brillouin zone were approximated by sums over a 10 × 10 × 8 mesh of special *k*-points according to the Monkhorst–Pack scheme.[23] Relaxation of the lattice parameters and the atomic positions was performed using a Broyden–Fletcher–Goldfarb–Shanno algorithm until the maximal residual force and pressure were less than 5×10^{-6} Ha Bohr^{-1} and 1×10^{-3} GPa, respectively. At the end of this structure relaxation, the calculated lattice parameters, a = 4.65 Å and c = 3.05 Å, were in excellent agreement with the experimental ones (see next section). Dynamical matrix, dielectric constants and Born effective charges are calculated within a variational approach to density functional perturbation theory (DFPT). Phonon dispersion curves were interpolated according to the scheme described by Gonze *et al.*[24] The dipole–dipole interactions were subtracted from the dynamical matrices before Fourier transformation, so that only the short-range part was handled in real space. We considered a 2 × 2 × 2 *q*-points grid for the calculation of the phonon band structure and a denser 100 × 100 × 100 grid was used for the calculation of the phonon density-of-states.

Experimental

Raman spectroscopy at high pressure

Raman experiments were carried out using a Horiba low frequency Labram Raman spectrometer operated with a 532 nm wavelength laser compatible with our high-pressure setup (Diamond Anvil Cell – DAC), which can detect an inelastic signal down to about 6 cm^{-1}. Laser power was set at 5 mW at the entrance of the DAC to avoid heating. The beam was focused on the sample using a 50× objective, with beam diameter ~2 μm at the sample. The scattered light was collected in backscattering geometry using the same objective.

High pressure was generated using a membrane DAC with low-fluorescence diamonds. Samples were placed into a 125 μm chamber drilled in an indented stainless-steel gasket. No pressure transmitting medium was used. The pressure was probed by the shift of the $R1$ fluorescence line of a small ruby chip.

Synthesis and characterization of $Ti_{0.5}Sn_{0.5}O_2$ nanoparticles at ambient conditions

Synthesis of $Ti_{0.5}Sn_{0.5}O_2$ nanoparticles has been described elsewhere.[25] In brief, 10 g of $[SnCl_4Ti(OEt)_4(EtOH)_2]$ were added to 100 mL of boiling water and stirred for 2 h. Addition of NH_4OH until pH 6–7 was reached led to the precipitation of a white powder which could be recovered by centrifugation, washed twice with de-ionized water and ethanol and finally dried at 70 °C for 12 h (4 g). The as-prepared particles were divided into two batches that were annealed following two different conditions, at 750 K during 4 h (batch 1) and at 1120 K during 2 h (batch 2). These temperatures have been chosen to obtain batches with significantly different sizes. Higher temperatures are prohibited as a spark plasma sintering treatment at 1370 K led to a demixing.[25] In the latter case, clear signature of appearance of TiO_2 and SnO_2 was reported

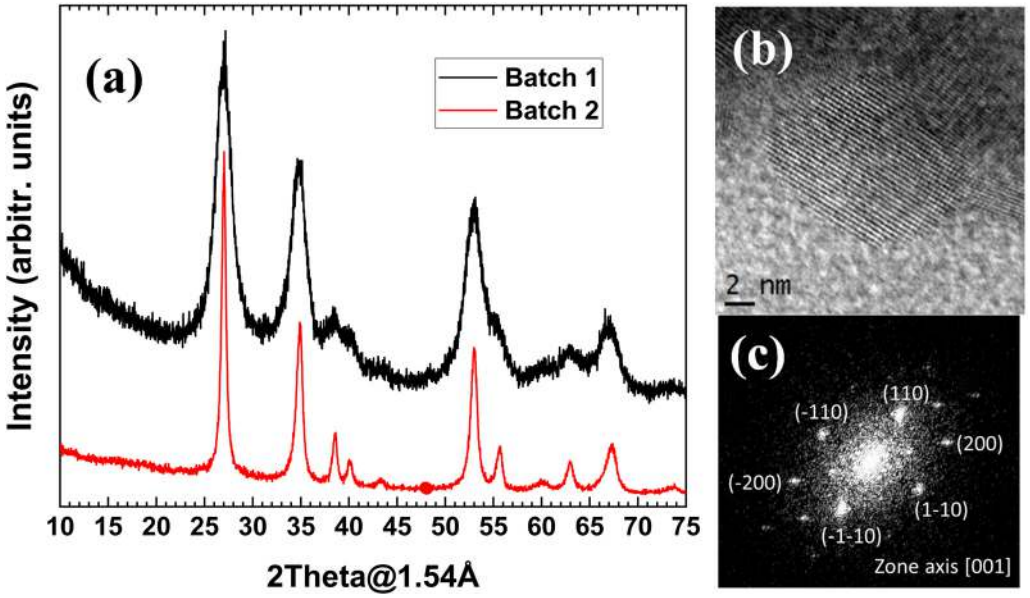

Fig. 1 (a) X-Ray diffractograms from batch 1 (treatment at 750 K during 4 h) and batch 2 (treatment at 1120 K during 2 h). (b) Typical TEM images obtained on batch 2. (c) Fast Fourier transform and indexation of the particle shown in (b).

by TEM and XRD.[25] In our present case, no trace of end-members has been observed.

According to X-Ray diffraction (Fig. 1a), and considering the nanoparticles are single-domain as verified by TEM (see below), the Scherrer equation indicates that the particle size of batch 1 is centered on 4 ± 1 nm whereas batch 2 has a particle size around 12 ± 1 nm. TEM analysis on this batch (Fig. 1b and c) allows obtaining the particle size distribution (see Fig. S1–3†) and to refine the particle size. It gives an average size of 5 ± 1 nm and 10 ± 2 nm for batch 1 and batch 2, respectively.

In both cases, the indexations of the X-ray diffraction pattern are in agreement with a rutile structure with cell parameters a = 4.67(1) Å and c = 3.07(1) Å. This corresponds to the expected parameters predicted by the Vegar's law *i.e.*, a linear combination of the end member cell parameters when considering a substitutional solid solution.[26,27] This observation is an indication that there is no demixing and no surface segregation as observed in some cases.[28] This difference may originate from the synthesis process using a single source precursor (SSP) and the different situations found in binary nanoparticles (solid solution, janus, core–shell).[29,30]

The Raman spectrum of batch 1 is shown in Fig. 2 along with spectra of end-member oxides, *i.e.*, TiO_2 and SnO_2, either as bulk (b) or nanostructure (n). It is worth noting that TiO_2 nanoparticles usually crystallizes in the anatase structure and no reference Raman spectrum of the rutile phase could be

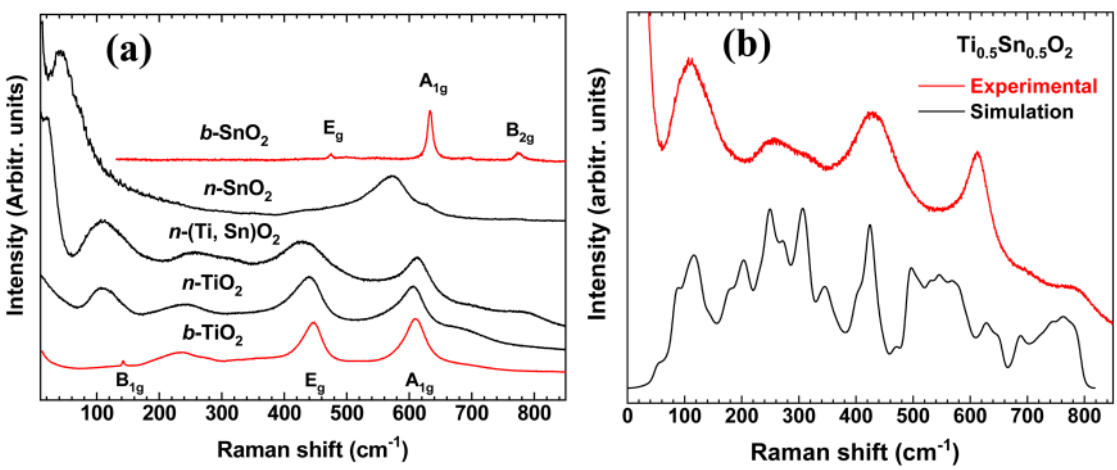

Fig. 2 (a) Comparison of the Raman spectra for nanostructures of n-SnO_2 (3 nm nanoparticles), n-TiO_2 (nanorods with 8 nm diameter from ref. 14) and n-$Ti_{0.5}Sn_{0.5}O_2$ (5 nm nanoparticles) along with Raman spectra of bulk TiO_2 and SnO_2 (b-TiO_2 and b-SnO_2). All samples adopt a rutile-type structure. In b-TiO_2, the B_{2g} mode is hardly detectable whereas in b-SnO_2, the B_{1g} is not observed (see text). (b) Comparison between experimental Raman spectra and simulated vibrational density of states (vDOS) for $Ti_{0.5}Sn_{0.5}O_2$.

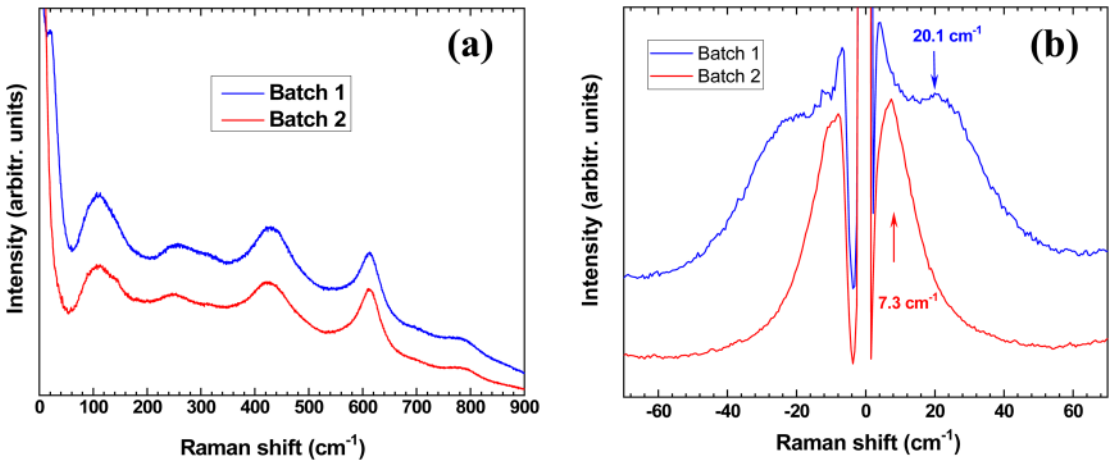

Fig. 3 Comparison of Raman spectra of batch 1 (mean particle size: 5 nm) and batch 2 (mean particle size: 10 nm). (a) Frequencies up to 900 cm^{-1}. (b) Zoom on frequencies below 60 cm^{-1}.

obtained with ultrafine nanoparticles. The reference spectrum for nanostructured rutile TiO_2 is therefore extracted from ref. 14, as nanorods with 8 nm-diameter were found to remain in the rutile structure.

The analysis of the vibrational representation of the normal modes at the center of the Brillouin zone[31] indicates that four Raman-active modes are expected for the rutile-type structure (A_{1g}, B_{1g}, B_{2g}, E_g). It has to be noted that in TiO_2, the B_{2g} mode is very weak. In SnO_2, the B_{2g} mode is visible but not the B_{1g} one, as supported by calculations.[32] For all these vibrational modes, the oxygen atoms vibrate while cations are at rest. As already discussed for TiO_2 nanorods, the large band at ~120 cm^{-1} is not expected according to the Raman selection rules but is originated by defects.[14] Indeed, the Raman selection rules are established for an infinite perfect crystal. The presence of defects (usually oxygen vacancies in oxides[33]) breaks the usual selection rules and gives access to forbidden vibrational modes and also to $k \neq 0$ modes, *i.e.*, modes in the Brillouin zone. Such effect is revealed by comparing the Raman spectra with the calculated vibrational density of states (vDOS) of the solid solution (Fig. 2b). The correspondence between the Raman peaks and the maxima of the simulated vDOS of the mixed system also confirms that there is no segregation *i.e.*, demixting between Ti-rich and Sn-rich compounds.

One observes that the spectrum of $Ti_{0.5}Sn_{0.5}O_2$ nanoparticles is very similar to that of TiO_2 in its rutile phase and rather different from nanometric rutile SnO_2. It is well documented that the Raman spectra of SnO_2 are strongly affected by the nanometrization with a strong broadening of the Raman peaks,[34,35] as it can be seen by comparing n-SnO_2 and b-SnO_2 in Fig. 2a. This effect can be discussed as resulting from the effect of defects on the decoupled anionic and cationic sublattices.[32] Thus, the interesting observation of the similarity between the $Ti_{0.5}Sn_{0.5}O_2$ and TiO_2 Raman spectra indicates that decoupling between sublattices is not observed in the solid solution (as it is in the case of SnO_2 nanoparticles) despite the presence of defects.

Raman spectra from both batches of nanoparticles are compared in Fig. 3. There is no strong difference except at low-frequency, below 40 cm^{-1}. In that spectral range, there is a defined peak in the case of batch 1. This peak located at ~20 cm^{-1} corresponds to the confined acoustic vibration in nanoparticles [ref. 36 and references therein]. As the frequency is inversely proportional to the radius of the particles in the Lamb's model,[37] this peak is hardly observed for batch 2 under ambient conditions. For this particle size (10 nm), the expected peak position should be located around ~8 cm^{-1}, which is the detection limit of this peak using this experimental configuration. This peak is hardly observable at ambient pressure but better observed with increasing pressure, as described in the following section. It is worth noting that the observation of these low-frequency peaks is an indication that the nanoparticles are free standing (in agreement with the TEM observations). They would not be observable if there was some sintering of the nanoparticles.

Results

$Ti_{0.5}Sn_{0.5}O_2$ – 5 nm

Raman spectra of 5 nm diameter nanoparticles (batch 1) under pressure are shown in Fig. 4. No phase transition can be observed up to 30.1 GPa, the highest pressure achieved in this run. It is worth noting that such extended stability is surprising as both TiO_2 and SnO_2, bulk or nanostructures, undergo phase transitions below 20 GPa. In the case of TiO_2 nanorods, phase transition towards a monoclinic phase (baddeleyite) occurs at ~16 GPa.[14] A similar transformation is observed for TiO_2 nanoparticles with anatase as the initial structure.[13,18] In SnO_2 nanoparticles, a pressure-induced disordering has been reported starting above 7 GPa with a disorder propagation from the shell to the core ending in the anionic sublattice amorphization above 19 GPa.[12]

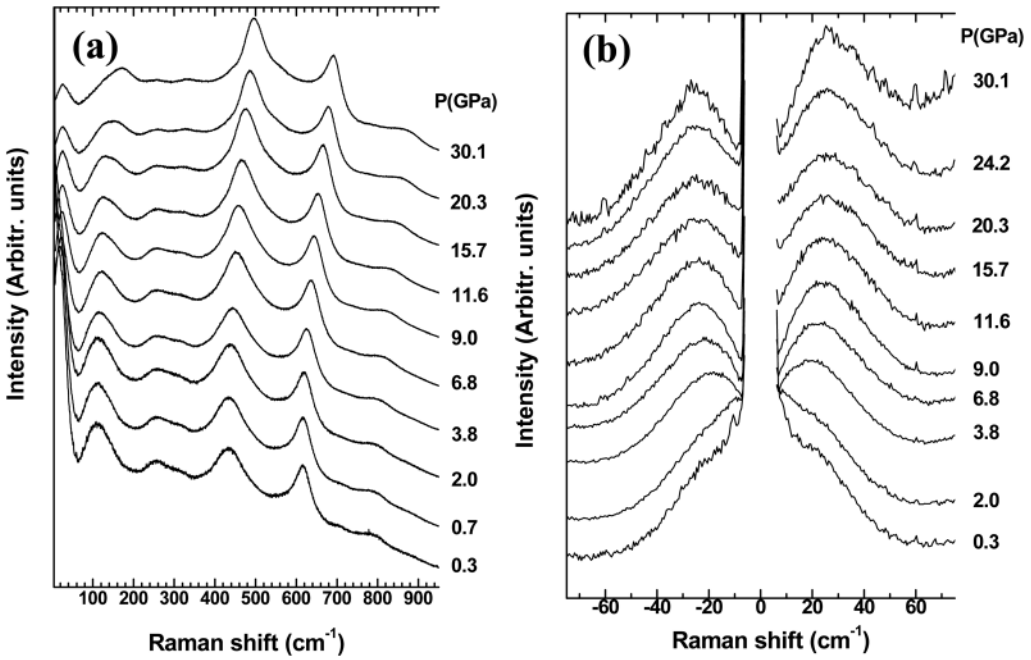

Fig. 4 (a) Raman spectra of $Ti_{0.5}Sn_{0.5}O_2$ of 5 nm (batch 1) with increasing pressure. (b) Low-frequency range recorded during the same experiment.

The pressure dependences of the Raman modes are indicated in Table 1 for both batches and for TiO_2 and SnO_2 nanostructures. The pressure-dependencies are closer to those observed in n-TiO_2 than in n-SnO_2. This seems to indicate a bond energy dominated by the Ti–O interaction.

The low-frequency peak (confined acoustic mode) can be clearly monitored above 3 GPa and shows a non-linear behavior with increasing pressure. This pressure-induced evolution (Fig. S4†) can be roughly divided into two regimes with increasing pressure. The first regime, up to ~12 GPa, can be approximated by a linear variation with pressure with a slope of 0.8 cm^{-1} GPa^{-1}. This value is close to the observed variation in SnO_2 nanoparticles but it should be noted that this value is not available for TiO_2 rutile nanoparticles. The second regime shows a drastic reduction of this variation and the peak position is apparently unaffected by the pressure application. This is related to the pressure-dependency of the sound velocity, as discussed in ref. 38.

The decompression shows a totally reversible path with a Raman spectrum after pressure cycling very similar to the Raman spectrum before compression (Fig. 5). The compaction induces a narrowing of the Rayleigh line allowing a better definition of the low-frequency Raman peak.

Table 1 Pressure-derivatives of the peak positions for the $Ti_{0.5}Sn_{0.5}O_2$ nanoparticles (batches 1 and 2) compared to those of SnO_2 [12] and TiO_2.[14] The label "disorder" corresponds to the band observed at 120 cm^{-1} (see text)

Symmetry	Batch 1	Batch 2	n-SnO_2 [12]	n-TiO_2 [14]
Disorder	1.1(1)	0.9(1)	—	1.1(1)
E_g	2.7(1)	2.8(1)	2.5(1)	2.8(1)
A_{1g}	3.2(1)	3.1(2)	4.6(1)	2.8(1)
B_{2g}	3.1(2)	2.9(1)	4.0(1)	—

$Ti_{0.5}Sn_{0.5}O_2$ – 10 nm

Using the same experimental set-up, high-pressure experiment was performed on batch 2. The Raman spectra during compression are shown in Fig. 6 and the pressure-dependencies of the peak positions are reported in Table 1. They are similar to that observed for batch 1. The low-frequency mode also shows a similar behavior (Fig. S5†). However, contrary to the previous experiment on batch 1, *i.e.* on smaller nanoparticles, a phase transition is observed between 20.3 and 25.1 GPa. It is worth noting that the low-frequency peak disappears at the transition confirming that this signal is clearly related to the sample and its low-pressure structure. The high-pressure phase is difficult to identify because of the broadness of the peaks. It may correspond to a highly disordered baddeleyite structure, as observed in pure TiO_2 nanostructures.[14] One may also interpret it as amorphous. However, on decompression, a crystalline structure is observed (Fig. 7). Usually, in TiO_2, the reported pressure-induced amorphization is irreversible.[17] Therefore, the high-pressure phase is probably not amorphous but highly disordered. It may result from a frustration in the transformation of the anionic sublattice. As a matter of fact, the high-pressure phases of TiO_2 and SnO_2 (modified fluorite) exhibit a distorted fcc cationic sublattice but the anionic arrays differ, leading to a metal coordination number of 7 in the baddeleyite structure (TiO_2) and 6 + 2 in the modified fluorite one (SnO_2).[39]

On decompression, the Raman spectra show some changes that are significant but are difficult to interpret because of the

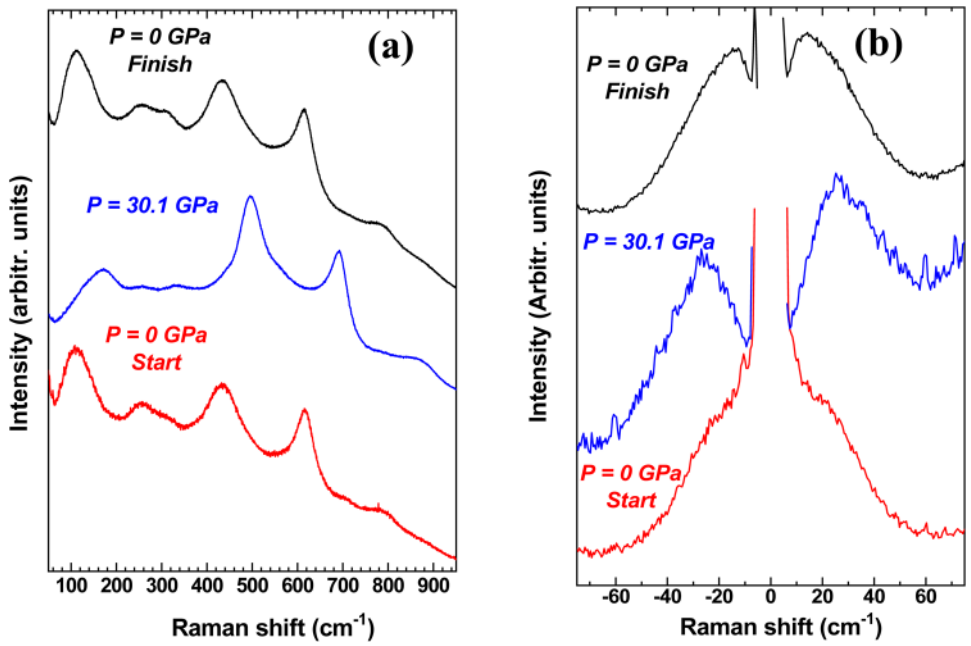

Fig. 5 (a) Raman spectra showing the entire pressure cycle from ambient pressure to the highest pressure reached in this experiment (30.1 GPa) and followed by decompression to ambient pressure. (b) Low-frequency range recorded during the same experiment.

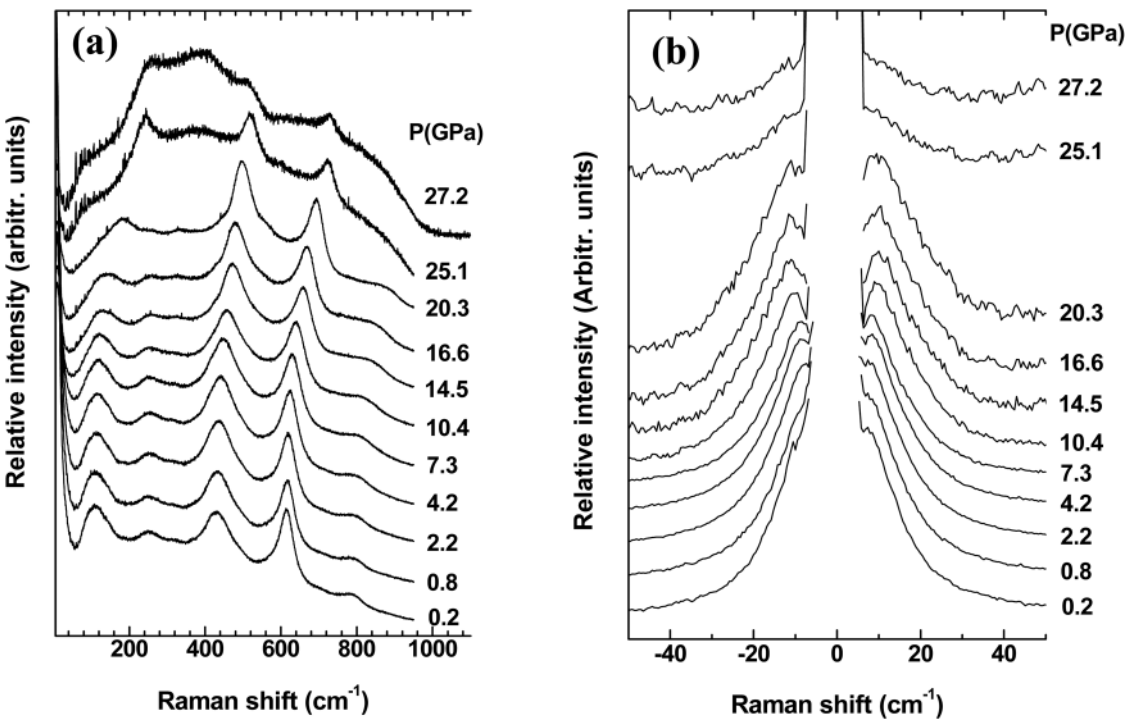

Fig. 6 (a) Raman spectra of $Ti_{0.5}Sn_{0.5}O_2$ of 10 nm (batch 2) with increasing pressure. (b) Low-frequency range recorded during the same experiment.

broadness of the Raman bands. Below 6.4 GPa a typical spectrum of the columbite (or α-PbO_2) structure (space group #60, *Pbcn*) is obtained. This orthorhombic structure is usually observed on bulk TiO_2 under increasing pressure, between the anatase and the baddeleyite phases. In nanostructures, this phase is bypassed during compression but is generally observed on decompression (Fig. S6†).[13,18] This phase is also observed in SnO_2 under pressure, but under non-hydrostatic

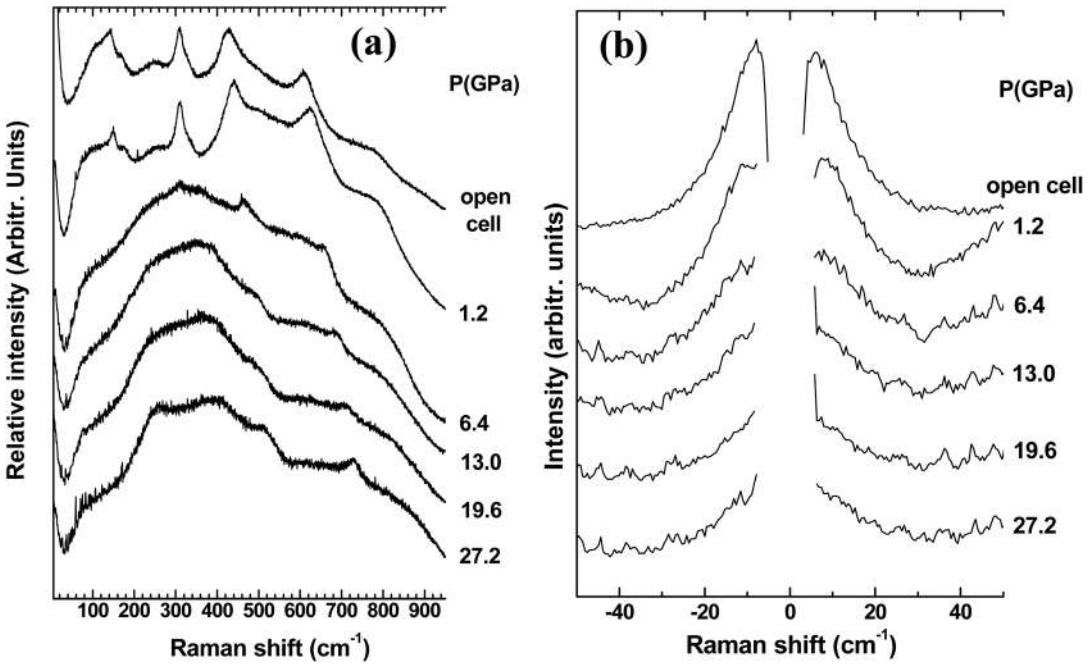

Fig. 7 (a) Raman spectra of $Ti_{0.5}Sn_{0.5}O_2$ of 10 nm (batch 2) with decreasing pressure. (b) Low-frequency range recorded during the same experiment.

conditions, and after a pressure cycle.[39] The α-PbO_2 phase is the kinetically preferred phase during the decompression and is retained as a metastable phase. This is due to orientational relationships that facilitate certain transition pathway as discussed in ref. 39.

In conclusion, for nanoparticles with a diameter centered at ~10 nm, an abrupt phase transition is observed above 20 GPa without preliminary disordering. The transformation to the high-pressure structure occurred above ~20 GPa in $Ti_{0.5}Sn_{0.5}O_2$ *vs.* ~16–18 GPa for the TiO_2 rutile nanorods or anatase nanoparticles.[13,14,18] On decompression, the recovered phase is the α-PbO_2 structure.

Discussion

In view of the experimental results reported in this work, there are at least two effects inducing an extended range of stability of the rutile phase: (i) a size effect as it clearly appears that the size plays a significant role in the phase transition and the stability field of the different phases involved; (2) the impact of the solid solution with respect to the end-members (TiO_2 and SnO_2).

First, the increase of the transition pressure with decreasing size is a general effect and has been documented. Generally, it results from two considerations (and their combination): kinetics and thermodynamics. Recent works has formalized the increase in stability at the nanoscale either by a classical (Gibbs) approach or using the Landau theory of phase transitions.[40] This is a $1/R$ scaling law showing that the transition pressure is shifted to a higher value with decreasing size and depending on the difference in interfacial energy between the low- and high-pressure phases. This is the case of SnO_2 nanoparticles: a pressure-induced phase transition to the high-pressure cubic phase is observed at 30 GPa for an 8 nm-particle while this transition pressure is 23 GPa for bulk SnO_2. For 3 nm particles, no phase transition is observed up to at least 39 GPa by X-ray diffraction techniques and the phase remains the rutile structure.[11] In TiO_2, no such clear $1/R$ dependence has been reported.

The kinetic effect can be described by the classical nucleation theory,[41] which shows that the nucleation of a phase leads to a gain of volumetric energy but at a cost of a surface energy. Therefore, the radius of a critical nucleus can be calculated and is usually on the order of a few nanometers. If this critical diameter is larger than the size of the nanoparticles, the nucleation of the new phase can be bypassed. In the case of anatase TiO_2, a kinetic effect has been proposed to explain the bypass of the intermediate columbite phase.[13] Thus, it has been shown that the pressure-induced transformation from anatase to columbite (α-PbO_2) requires a nucleus of ~12 nm. The critical size of the nucleus is ~4 nm for the next high-pressure baddeleyite phase,[13] the one that is usually observed in nanomaterials of critical size (diameter of the nanoparticle or diameter of the rods) less than 10 nm (ref. 13, 14, 16 and 18) and with a low density of defects.[13,18]

In the case of $Ti_{0.5}Sn_{0.5}O_2$, the observation of a pressure-induced phase transition for the 10 nm nanoparticles above ~20 GPa but no phase transition for those of 5 nm, at least up to ~30 GPa, indicates that the trends is similar to SnO_2 with a size dependence on the transition pressure, a situation not observed in nanostructured TiO_2.

Defects and surface chemistry also influence structural stability. The different annealing temperatures of the as-prepared particles to obtain batch 1 (750 K) and batch 2 (1120 K) can induce certain modifications in the concentration of defects and the surface chemistry. However, it has been shown that defects have a destabilizing effect on the crystallographic structure leading to pressure-induced disordering (ultimately amorphization) and a decrease of the transition pressure.[9,18,42] Moreover, this effect is all the more marked as the particles are small. This is not what is observed in this study where the smallest particles show the greatest stability. This seems to indicate that the surface chemistry and the associated defects are not the essential parameters driving the structural stability (destabilization) of the nanoparticles.

The second stabilizing effect is linked to the solid solution. Indeed, while no phase transition has been reported using X-ray diffraction which mainly probes the cationic sub-lattice, a pressure-induced disordering has been observed in SnO_2 nanoparticles and SnO_2 bulk in using Raman spectroscopy.[12,32] This characterization technique is more sensitive to the anionic sub-lattice. Indeed, a pressure-induced disordering of the oxygen sublattice starting above 7 GPa in 3 nm particles was evidenced, with the propagation of the disorder from the shell to the core.[12] Such disordering ultimately induced an oxygen sub-lattice amorphization at $P \sim 19$ GPa (Fig. 8). Likewise, it was recently shown that bulk SnO_2 also exhibits such a decoupling of cationic and anionic sublattices under pressure.[32] The oxygen sublattice in bulk SnO_2 indeed transforms to a disordered array while the cationic sub-lattice shows no transformation. Such behavior is similar to what is observed in nanoparticles. It has also been shown that a critical defect density (mainly oxygen vacancies) destabilizes the anionic sublattice without significantly affecting the metallic sublattice in SnO_2. These observations indicate a general property associated to this material, *i.e.*, a tendency to have a decoupling between cationic and anionic sublattices.[32]

In the case of anatase TiO_2, such effect of disordering is to a certain extent observed for nanoparticles smaller than 10 nm and exhibiting a critical defect density.[16,42] The difference with SnO_2 is that the two sublattices, anionic and cationic, undergo a disordering at the phase transition around 18–20 GPa, leading to a complete amorphization (Fig. 8).[15–17] Thus, in TiO_2 nanostructures (with anatase or rutile structure), a pressure-induced phase transition – towards disordered baddeleyite or an amorphous state, depending on size and surface state of the particles – is always observed below 20 GPa without clear $1/R$ variation.[13,16,18]

In the case of $Ti_{0.5}Sn_{0.5}O_2$, the decoupling of the sublattices reported for SnO_2 is not observed even at high pressure despite the presence of defects, as evidenced by Raman spectroscopy. Therefore, the solid solution $Ti_{0.5}Sn_{0.5}O_2$ shows an extended stability at the nanoscale, both of its cationic and anionic sublattices, which is highly unusual and unexpected compared to the end members (Fig. 8).

This result can be interpreted in an original perspective of the description of phase transition which has been recently

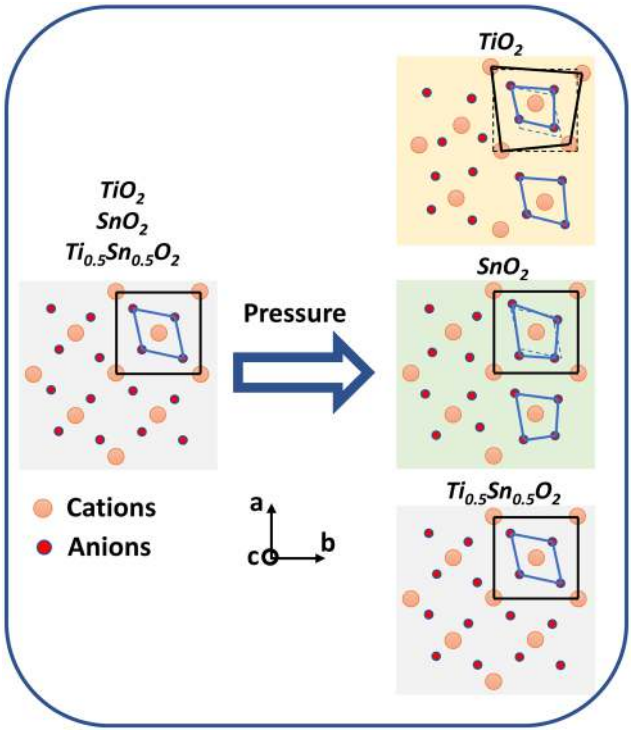

Fig. 8 Structural representation along the *c*-axis of the initially rutile phase. The structure is identical at ambient pressure for SnO_2, TiO_2 and $Ti_{0.5}Sn_{0.5}O_2$ differing only by the value of their cell parameters. Under pressure, in the presence of defects, TiO_2 nanoparticles undergo amorphization with the disordering of both cationic and anionic sublattices. In SnO_2, the cationic sublattice provides structural stability, and only the oxygen sublattice experiences such a disordering because of a weaker Sn–O bonding. In $Ti_{0.5}Sn_{0.5}O_2$, the Sn ensures the structural stability as in SnO_2. The coupling between the cations and the anions is stronger due to the Ti–O bonds, leading to extreme structural stability.

brought to date.[43] The traditional crystallographic description of the structure of ionic crystals relies on the packing of fundamental building blocks generally considered to be a cation-centered polyhedron. This description is generally associated with Pauling's rules.[20] This picture implicitly assumes a strong coupling between the cationic and anionic sublattices. An alternative approach to the description of the structure was proposed by O'Keeffe and Hyde in the mi-80s:[44] the oxide structures are described in terms of their cation packings and the coordination of the anions by these cations. In other words, instead of considering a structure as a regular anionic lattice into which cations have been inserted, the alternative is used, namely the insertion of anions into a regular cation array.[44,45] Later, this idea was reintroduced through the "anions in metallic matrices" model, where a crystal structure of an inorganic compound can be described as a metallic matrix in which geometric and electronic structures govern the localization of the anions in the lattice.[46] The results obtained on SnO_2 under high-pressure can be interpreted in this framework: the Sn cation lattice ensures stability over a wide pressure range. However, since there is a weak coupling

between cationic and anionic sublattices, the oxygen sublattice with an initial critical defect density evolves differently. Under pressure, the defect density increases until percolation and amorphization of the anionic network occur.[32] This effect has recently been confirmed by a combination of XRD and EXAFS.[47]

The effect of decoupling between the two sublattices has been observed in pressure-induced phase transitions in complex structures of rare earth molybdates ($RE(MoO_4)_3$ with RE = Gd, Eu, Tb, Nd), for which two-step amorphization has been reported regardless of the form of the samples. The anionic sublattice begins to exhibit amorphous-like Raman, photoluminescence, or EXAFS signatures at a pressure lower than that of the cationic sublattice probed by X-ray diffraction.[48,49] Partial (sublattice) amorphization has also been discussed in $Co(OH)_2$, where infrared spectroscopy reported a disordering of the O–H sublattice.[50] In Ga_2O_3, the β-to-α pressure-induced phase transition is accompanied by a strong broadening of the Raman signal while X-ray diffraction patterns do not indicate such a disordering in the cationic sublattice.[51]

The rutile structure is particularly suited to such studies of a particular sublattice, since only oxygen atoms are involved in the Raman-active vibrational modes.[52] The rutile structure consists of a body centered tetragonal (bct) cationic array. This is the atomic arrangement found in the high-pressure γ-Sn allotrope[53,54] which is stable over a large range of pressure (from 10 to 31 GPa) showing only slight distortion to a body-centered orthorhombic structure (bco) above 32 GPa and to a bcc lattice above 40 GPa.[54] In the case of Ti, the bct packing is metastable and is only observed under non-hydrostatic pressure [ref. 55 and refs therein]. However, the high-pressure hexagonal phase ω can be related to a distorted bcc structure.[55]

According to the model proposed by Bain, bct is the intermediate structure in the bcc-to-fcc transformation. Pressure should favor the fcc due to its higher compacity in a hard sphere model, a situation found for the TiO_2 and SnO_2 oxides as the high-pressure phases observed either in TiO_2 (baddeleyite) or SnO_2 (distorted fluorite) correspond to distorted fcc cationic sublattices.[39,56] However, this situation in not found in Sn and Ti, where the bcc packing is stable under pressure. This stability of bcc packing under pressure has been discussed by Oganov *et al.*[57] in the case of calcium. This can be understood by the fact that bcc is the most compact structure because of shorter bond length *i.e.*, the sphere diameter is not the same in the bcc or in the fcc packing. In some sense, this configuration corresponds to the packing of interpenetrating spheres (shorter distance if the diameter is fixed) for which the bcc has the highest density.[58]

Therefore, a possible explanation of the stability of the SnO_2 nanoparticles is the following: in bulk SnO_2, the oxygen atoms prevent the interpenetration of cations (as in the case of pure Sn) which leads to a hard sphere behavior under pressure *i.e.*, a transformation to a fcc arrangement of the cations (distorted fluorite). In the case of nanoparticles, the surface and the deficit of oxygen does not play this role of buffer between cations leading to a higher stability of the bct or bcc structure as it is observed in the elemental Sn under pressure. Therefore, the smaller the nanoparticles, the higher the effect of surface and oxygen vacancies, and the bcc packing is stable as in the case of pure Sn. Therefore, the size-dependent stability of the rutile phase may be related to the stability of the cationic bcc lattice under pressure.

On the other hand, the absence of disordering of the oxygen sublattice in $Ti_{0.5}Sn_{0.5}O_2$ nanoparticles is the index of a stronger coupling between the sublattices unlike in SnO_2 nanoparticles. This effect most likely originates in the difference in cohesive energy (much lower in SnO_2 than in TiO_2) which reflects the energy of metal–ligand bonds.[59] This effect explains why the Raman spectrum of $Ti_{0.5}Sn_{0.5}O_2$ resembles that of TiO_2 (Fig. 2a). The main peaks of the rutile structure are only slightly affected unlike the case of SnO_2 which shows a completely different Raman spectrum affected by the defects.[34,35] This indicates a privileged coupling between the Ti and O sublattices.

Therefore, the extreme stability observed in ultrafine $Ti_{0.5}Sn_{0.5}O_2$ nanoparticles can be interpreted as the result of a synergistic effect between Sn and Ti atoms. Sn provides a size-dependency on the stability field and Ti induces a strong coupling between anionic and cationic sublattices, preventing the propagation of the disorder in the oxygen sublattice. In other words, each cation plays a respective role: Sn ensures the stability of the metallic sublattice with respect to pressure and Ti ensures the stability of the oxygen sublattice.

Conclusions

This work highlights the enhanced structural stability of the TiO_2–SnO_2 system at the nanoscale. Under pressure, the ~5 nm particles show no phase transformation up to ~30 GPa. In the case of end-members, phase transitions are observed in the range 16–20 GPa. 3 nm SnO_2 nanoparticles exhibit a sublattice disordering starting from 7 GPa and ending at around 19 GPa, and the TiO_2 nanoparticles transform to a high-pressure phase at $P \sim$ 16–18 GPa. For $Ti_{0.5}Sn_{0.5}O_2$ nanoparticles of ~10 nm, a phase transition is observed between 20 and 25 GPa.

The size dependence of the transition pressure is similar to what is observed in pure SnO_2. However, no pressure-induced disordering of the anionic sublattice was observed, contrary to what is observed in the SnO_2 nanoparticles. The experimental pieces of evidence are explained as follows: Ti cations introduce coupling between cationic and anionic sublattices (stronger metal–ligands bonds) and Sn cations improve the structural stability of the cationic sublattice. This leads to a synergistic effect to which the presence of the two atoms provides enhanced structural stability by counterbalancing their effects. This finding paves the way to the development of new nanomaterials that exhibit improved properties by selecting the favorable contribution of each component, similar to what is

proposed with metamaterials. These materials are composites made of constituent materials, leading to effective medium properties beyond those of their ingredients.[60] In our case, the mixture of two cations leads to a structural stability well beyond those of TiO_2 and SnO_2 components.

Conflicts of interest

There are no conflicts to declare.

Acknowledgements

The authors acknowledge the Consortium Lyon Saint-Etienne (CLYM) for the access to the electron microscope and the CECOMO and PLECE platforms at Université Lyon 1 for the use of the spectrometer and of the Diamond Anvil Cells, respectively.

References

1 D. Machon, V. Pischedda, S. Le Floch and A. San-Miguel, *J. Appl. Phys.*, 2018, **124**, 160902.
2 S. Illy, O. Tillement, F. Machiz, J. M. Dubois, F. Massicot, Y. Fort and J. Ghanbaja, *Philos. Mag. A*, 1999, **79**, 1021–1031.
3 A. Navrotsky, *Geochem. Trans.*, 2003, **4**, 34–37.
4 P. Buffat and J. P. Borel, *Phys. Rev. A*, 1976, **13**, 2287.
5 N. Gaston, *Adv. Phys.: X*, 2018, **3**, 1401487.
6 S. H. Tolbert and A. P. Alivisatos, *Annu. Rev. Phys. Chem.*, 1995, **46**, 595–626.
7 A. San-Miguel, *Chem. Soc. Rev.*, 2006, **35**, 876–889.
8 F. Bai, K. Bian, X. Huang, Z. Wang and H. Fan, *Chem. Rev.*, 2019, **119**, 7673–7717.
9 D. Machon and P. Mélinon, *Phys. Chem. Chem. Phys.*, 2015, **17**, 903.
10 J. Haines, J. M. Léger and O. Schulte, *Science*, 1996, **271**, 629.
11 Y. He, J. F. Liu, W. Chen, Y. Wang, H. Wang, Y. W. Zeng, G. Q. Zhang, L. N. Wang, J. Liu, T. D. Hu, H. Hahn, H. Gleiter and J. Z. Jiang, *Phys. Rev. B: Condens. Matter Mater. Phys.*, 2005, **72**, 212102.
12 H. T. Girão, T. Cornier, S. Daniele, R. Debord, M. A. Caravaca, R. A. Casali, P. Mélinon and D. Machon, *J. Phys. Chem. C*, 2017, **121**, 15463.
13 G. R. Hearne, J. Zhao, A. M. Dawe, V. Pischedda, M. Maaza, M. K. Nieuwoudt, P. Kibasomba, O. Nemraoui and J. D. Comins, *Phys. Rev. B: Condens. Matter Mater. Phys.*, 2004, **70**, 134102.
14 D. Machon, N. Le Bail, P. Hermet, T. Cornier, S. Daniele and S. Vignoli, *J. Phys. Chem. C*, 2018, **123**, 1948–1953.
15 V. Pischedda, G. R. Hearne, A. M. Dawe and J. E. Lowther, *Phys. Rev. Lett.*, 2006, **96**, 035509.
16 V. Swamy, A. Kuznetsov, L. S. Dubrovinsky, P. F. McMillan, V. B. Prakapenka, G. Shen and B. C. Muddle, *Phys. Rev. Lett.*, 2006, **96**, 135702.
17 D. Machon, M. Daniel, V. Pischedda, S. Daniele, P. Bouvier and S. Le Floch, *Phys. Rev. B: Condens. Matter Mater. Phys.*, 2010, **82**, 140102.
18 D. Machon, M. Daniel, P. Bouvier, S. Daniele, S. Le Floch, P. Mélinon and V. Pischedda, *J. Phys. Chem. C*, 2011, **115**, 22286.
19 G. Radnóczi, E. Bokányi, Z. Erdélyi and F. Misják, *Acta Mater.*, 2017, **123**, 82–89.
20 L. Pauling, *J. Am. Chem. Soc.*, 1929, **51**, 1010–1026.
21 X. Gonze, B. Amadon, P. M. Anglade, *et al.*, *Comput. Phys. Commun.*, 2009, **180**, 2582.
22 J. P. Perdew and Y. Wang, *Phys. Rev. B: Condens. Matter Mater. Phys.*, 1992, **45**, 13244.
23 H. J. Monkhorst and J. D. Pack, *Phys. Rev. B: Solid State*, 1976, **13**, 5188.
24 X. Gonze, J. C. Charlier, D. C. Allan and M. P. Teter, *Phys. Rev. B: Condens. Matter Mater. Phys.*, 1994, **50**, 13035.
25 S. Mishra, E. Jeanneau, S. Mangematin, H. Chermette, M. Poor Kalhor, G. Bonnefont, G. Fantozzi, S. Le Floch, S. Pailhes and S. Daniele, *Dalton Trans.*, 2015, **44**, 6848.
26 L. Vegard, *Z. Phys.*, 1921, **5**, 17; *Z. Kristallogr.*, 1928, **67**, 239.
27 A. R. Denton and N. W. Ashcroft, *Phys. Rev. A*, 1991, **43**, 3161–3164.
28 J. Miagava, A. Rubbens, P. Roussel, A. Navrotsky, R. H. R. Castro and D. Gouvêa, *J. Am. Ceram. Soc.*, 2016, **99**, 631–637.
29 X. Bouju, E. Duguet, F. Gauffre, C. R. Henry, M. L. Kahn, P. Mélinon and S. Ravaine, *Adv. Mater.*, 2018, **30**, 1706558.
30 L. Trotochaud and S. W. Boettcher, *Chem. Mater.*, 2011, **23**, 4920–4930.
31 S. P. S. Porto, P. A. Fleury and T. C. Damen, *Phys. Rev.*, 1967, **154**, 522–526.
32 H. T. Girao, P. Hermet, B. Masenelli, J. Haines, P. Mélinon and D. Machon, *Phys. Rev. Lett.*, 2018, **120**, 265702.
33 F. Gunkel, D. V. Christensen, Y. Z. Chen and N. Pryds, *Appl. Phys. Lett.*, 2020, **116**, 120505.
34 L. Abello, B. Bochu, A. Gaskov, S. Koudryavtseva, G. Lucazeau and M. Roumyantseva, *J. Solid State Chem.*, 1998, **135**, 78–85.
35 C. Xie, L. Zhang and C. Mo, *Phys. Status Solidi A*, 1994, **141**, K59–K61.
36 L. Saviot, D. Machon, A. Mermet, D. B. Murray, S. Adichtchev, J. Margueritat, F. Demoisson, M. Ariane and M. C. Marco de Lucas, *J. Phys. Chem. C*, 2012, **116**, 22043.
37 H. Lamb, *Proc. London Math. Soc.*, 1881, **s1–13**, 189–212.
38 A. Girard, J. Ramade, J. Margueritat, D. Machon, L. Saviot, F. Demoisson and A. Mermet, *Nanoscale*, 2010, **10**, 2154.
39 J. Haines and J. M. Léger, *Phys. Rev. B: Condens. Matter Mater. Phys.*, 1997, **55**, 11144.
40 D. Machon, L. Piot, D. Hapiuk, B. Masenelli, F. Demoisson, R. Piolet, M. Ariane, S. Mishra, S. Daniele, M. Hosni, N. Jouini, S. Farhat and P. Mélinon, *Nano Lett.*, 2014, **14**, 269.
41 H. J. Maris, *C. R. Phys.*, 2006, **7**, 946.

42 L. Piot, S. Le Floch, T. Cornier, S. Daniele and D. Machon, *J. Phys. Chem. C*, 2013, **117**, 11133.

43 A. Vegas, *Structural models of inorganic crystals: From the elements to the compounds*, Editorial Universitat Politècnica de València, València, 2018.

44 M. O'Keeffe and B. G. Hyde, An alternative approach to non-molecular crystal structures with emphasis on the arrangements of cations, in *Cation Ordering and Electron Transfer. Structure and Bonding*, Springer, Berlin, Heidelberg, vol. 61, 1985.

45 N. L. Ross and G. D. Price, in *The Stability of Minerals*, ed. G. D. Price and N. L. Ross, The Mineralogical Society Series, Springer, Dordrecht, 1992, vol 3.

46 Á. Vegas, D. Santamaría-Pérez, M. Marqués, M. Flórez, V. García Baonza and J. M. Recio, *Acta Crystallogr., Sect. B: Struct. Sci.*, 2006, **62**, 220.

47 D. Sneed, J. S. C. Kearney, D. Smith, J. S. Smith, C. Park and A. Salamat, *J. Synchrotron Radiat.*, 2019, **26**, 1245.

48 O. Le Bacq, D. Machon, D. Testemale and A. Pasturel, *Phys. Rev. B: Condens. Matter Mater. Phys.*, 2011, **83**, 214101.

49 D. Machon, V. P. Dmitriev, V. V. Sinitsyn and G. Lucazeau, *Phys. Rev. B: Condens. Matter Mater. Phys.*, 2004, **70**, 094117.

50 J. H. Nguyen, M. B. Kruger and R. Jeanloz, *Phys. Rev. Lett.*, 1997, **78**, 1936.

51 D. Machon, P. F. McMillan, B. Xu and J. Dong, *Phys. Rev. B: Condens. Matter Mater. Phys.*, 2006, **73**, 094125.

52 P. Merle, J. Pascual, J. Camassel and H. Mathieu, *Phys. Rev. B: Condens. Matter Mater. Phys.*, 1980, **21**, 1617.

53 D. Santamaria-Pérez, A. Vegas and U. Müller, *Solid State Sci.*, 2005, **7**, 479.

54 A. Salamat, R. Briggs, P. Bouvier, S. Petitgirard, A. Dewaele, M. E. Cutler, F. Corà, D. Daisenberger, G. Garbarino and P. F. McMillan, *Phys. Rev. B: Condens. Matter Mater. Phys.*, 2013, **88**, 104104.

55 A. Vegas, J. Mejía-López, A. H. Romero, M. Kiwi, D. Santamaría-Pérez and V. G. Baonza, *Solid State Sci.*, 2004, **6**, 809.

56 J. Haines, J. M. Léger, A. S. Pereira, D. Häusermann and M. Hanfland, *Phys. Rev. B: Condens. Matter Mater. Phys.*, 1999, **59**, 13650.

57 A. R. Oganov, Y. Ma, Y. Xu, I. Errea, A. Bergarad and A. O. Lyakhov, *Proc. Natl. Acad. Sci. U. S. A.*, 2010, **107**, 7646.

58 M. Iglesias-Ham, M. Kerber and C. Uhler, Sphere packing with limited overlap, in *Online Proceedings of the Canadian Conferece on Computational Geometry*, 2014.

59 N. I. Medvedevva, P. Zhukovm, Y. A. Khodos and V. A. Gubanov, *Phys. Status Solidi B*, 1990, **160**, 517.

60 M. Kadic, G. W. Milton, M. van Hecke and M. Wegener, *Nat. Rev. Phys.*, 2019, **1**, 199.